




Magnetic structure and resistivity minimum in GdCuAs₂

A. Balodhi ¹, J.-W. Kim,² D. Evans,³ A. Seepersad,¹ J. M. Grummer,¹ E. D. Mun ³ and M. G. Kim ¹

¹*Department of Physics, University of Wisconsin–Milwaukee, Milwaukee, Wisconsin 53201, USA*

²*Advanced Photon Source, Argonne National Laboratory, Argonne, Illinois 60439, USA*

³*Department of Physics, Simon Fraser University, Burnaby, British Columbia, Canada V5A 1S6*



(Received 31 May 2023; accepted 6 December 2023; published 19 December 2023)

The electrical resistivity of GdCuAs₂ single crystals exhibits an anomalous Kondo-like resistivity minimum above the antiferromagnetic ordering temperature $T_{N_1} \approx 10.6$ K, which is unusual for a highly localized $4f$ -moment (Gd³⁺) system. Using x-ray resonant magnetic scattering, we determined the magnetic structure of GdCuAs₂, where Gd moments are antiferromagnetically aligned along the crystallographic **a** axis and in the (+ + −) arrangement in the **c** direction and ferromagnetically arranged in the **b** direction. The antiferromagnetic order appears first at $\mathbf{q} = (\delta, 0, 0.5)$ below 10 K, with an incommensurate modulation along the **a** axis and locks into a commensurate position at $\mathbf{q} = (1/3, 0, 0.5)$ below $T_{N_2} \approx 6$ K. Our high-resolution x-ray diffraction measurements show a two-peak structure at $\mathbf{Q} = (2, 0, 6)$ above the resistivity minimum, suggesting a lower-symmetry crystal structure than the reported tetragonal structure, and the $\mathbf{Q} = (2, 0, 6)$ peak becomes a sharp one-peak structure below the resistivity minimum, implying a magnetoelastic coupling above T_N . Our findings suggest a complex interplay between the crystal structure and antiferromagnetic structure through a magnetoelastic coupling, associated with the anomalous resistivity minimum above T_{N_1} .

DOI: [10.1103/PhysRevB.108.224425](https://doi.org/10.1103/PhysRevB.108.224425)

I. INTRODUCTION

Metals are extensively studied and well-understood objects in condensed matter physics [1,2]. However, a class of materials known as strange metals, which exhibit behavior that is not entirely consistent with conventional metals, exists. One of the most well-known types of strange metals is superconductors, which demonstrate a complete disappearance of electrical resistivity [3,4]. Another type of strange metal behaves quite oppositely, showing an anomalous increase in electrical resistivity at very low temperatures, and has been the subject of considerable interest. The resistivity minimum (RM), a phenomenon characterized by an upturn in electrical resistivity, was first reported in materials containing dilute magnetic elements due to the Kondo effect [5–7]. Since then, the RM has been observed in a variety of different materials, including concentrated magnets [8,9], metallic glasses [10–13], bulk ceramics [14], and epitaxially grown films [15–18]. However, the mechanisms underlying this class of strange metals are not well understood, with only a few proposed explanations, such as spin-polarized tunneling [14,19], Kondo-like effects [20], and magnetic polaron formation [21–24].

The lack of electron-scattering mechanisms at low temperatures suggests that magnetism may play a critical role in the unusual RM in strange metals. A recent theoretical study indicated that in some materials, a highly frustrated Ruderman-Kittel-Kasuya-Yosida (RKKY) interaction may produce a classical spin liquid state, enhancing the backscattering process and generating a resistivity upturn (i.e., RM) at low temperatures [25]. In this model, the liquidlike spin state may appear as broad diffuse scatterings in the inelastic neutron scattering, and an increase in correlation length should accompany the RM produced by the RKKY mechanism. This

theory suggests that certain $RCuAs_2$ compounds may fall into this category, resulting in the RM just before the Néel order. Indeed, the RM has been observed in $RCuAs_2$, with $R = Nd, Sm, Gd, Tb,$ and Dy , just before the long-range antiferromagnetic (AFM) ordering [26–28].

To understand the RM in this family of compounds, knowledge of the crystal and magnetic structures and their behavior at low temperatures is required. Previous studies on polycrystalline samples showed that $RCuAs_2$ crystallizes in a tetragonal $P4/nmm$ structure at room temperature [26,27,29–31], as shown in Fig. 1(a). This family of materials has been considered for Peierls instability and consequent distortions. An effort to discover Peierls distortion has been unsuccessful except for one report arguing a monoclinic $P12_1/m1$ structure at room temperature [32]. And the crystal structures of this family have not been investigated at low temperatures. In particular, doping at the As site can transform the structure into an orthorhombic $Pmmn$ structure in slightly P-doped GdCuAs₂ [29,30], which might be the realization of enhanced Peierls instability.

Earlier, the AFM ground states of various $RCuAs_2$ were studied using neutron powder diffraction (NPD) measurements [33]. The magnetic structure of PrCuAs₂, which does not exhibit RM, suggests that the Pr spins align along the **c** axis with AFM coupling expressed by $\mathbf{q} = (0.5, 0, 0.5)$. However, the spin arrangement along the **c** axis was not determined due to the inherent limitation of the NPD technique. NdCuAs₂ and DyCuAs₂, both of which exhibit the RM, were found to have spins pointing in the **ab** plane with $\mathbf{q} = (0.5, 0, 0.5)$, but their **c**-axis spin arrangements were not determined. TbCuAs₂ (exhibiting the RM) and HoCuAs₂ (RM unknown) were found to have a complex incommensurate magnetic ordering with propagation vectors $\mathbf{q}_1(\text{Tb}) = (0.240, 0.155, 0.48)$

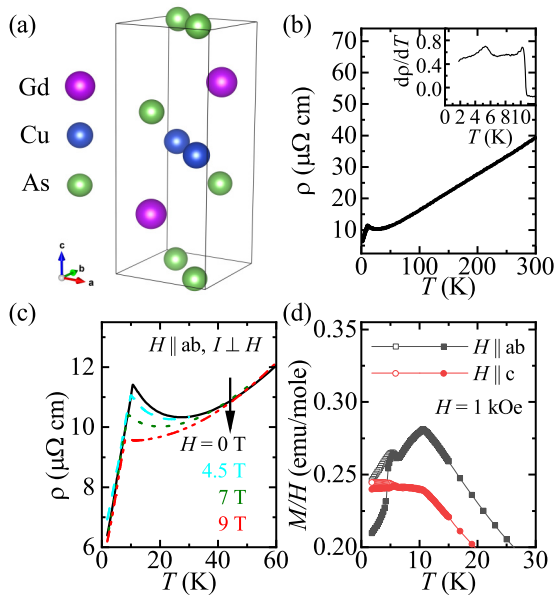


FIG. 1. (a) Crystal structure of GdCuAs_2 . The solid gray box marks the structural unit cell. (b) Temperature dependence of the electrical resistivity at $H = 0$ T. $d\rho/dT$ in the inset shows anomalies in the resistivity below 12 K. (c) Temperature dependence of the electrical resistivity at selected magnetic fields for $\mathbf{H} \parallel \mathbf{ab}$ and $\mathbf{I} \perp \mathbf{H}$. (d) Magnetic susceptibility at $H = 1$ kOe for $\mathbf{H} \parallel \mathbf{ab}$ and $\mathbf{H} \parallel \mathbf{c}$. Solid (open) symbols indicate the data taken while warming (cooling).

and $\mathbf{q}_2(\text{Tb}) = (0.205, 0.115, 0.28)$ and $\mathbf{q}(\text{Ho}) = (0.121, 0.041, 0.376)$, respectively, but their exact magnetic structures were not determined.

We investigate the structural and magnetic properties of GdCuAs_2 using single-crystal x-ray diffraction (SXD) and x-ray resonant magnetic scattering (XRMS). Our analysis indicates that the Gd moments align antiferromagnetically in the \mathbf{a} axis and the $(++--)$ arrangement in the \mathbf{c} axis and a ferromagnetic (FM) arrangement along the \mathbf{b} direction. The magnetic order appears incommensurate at $\mathbf{q} = (\delta, 0, 0.5)$ below 10 K and locks into a commensurate position at $\mathbf{q} = (1/3, 0, 0.5)$ at $T \approx 6$ K. We find that the crystal structure of GdCuAs_2 has a lower symmetry with different lattice parameters a and b , different from the reported tetragonal structure. The observed magnetic structure is consistent with the lower-symmetry crystal structure. We also observe an interesting response in the lattice parameters of GdCuAs_2 near the magnetic transitions and around the temperature where the resistivity minimum occurs. Lattice parameters a and b increase at $T \leq 30$ K, where the RM appears (T_{\min}), and lattice parameter c also shows a slight upturn or a plateau at a similar temperature. Furthermore, we find that the difference between lattice parameters a and b decreases below T_{\min} . We discuss possible mechanisms for the resistivity minimum and their connection to magnetoelastic coupling.

II. EXPERIMENT

Single crystals of GdCuAs_2 were grown out of a ternary melt with excess As and Gd [28]. The constituent elements of high-purity Gd, Cu, and As, taken in the ratio

$\text{Gd}_{0.04}(\text{Cu}_{0.5}\text{As}_{0.5})_{0.96}$, were loaded in an alumina crucible and sealed in a silica ampoule under partial argon pressure. Initially, the ampoule was heated slowly to 500°C in a box furnace, the temperature was maintained for 5 h, and then the ampoule was finally heated to 1050°C over 24 h. After being held for 2 h at 1050°C , the ampoule was slowly cooled down to 850°C over 100 h. After removing the excess liquid by centrifuging, shiny single crystals were obtained.

The phase purity of the samples from the growth batch was examined by x-ray powder diffraction using a Rigaku Miniflex at room temperature. DC magnetization was measured using a Quantum Design magnetic property measurement system, and temperature-dependent AC ($f = 16$ Hz) electrical resistance data were collected using a Quantum Design physical properties measurement system.

Temperature-dependent, high-resolution SXD and XRMS measurements were performed on a six-circle diffractometer on beamline 6-ID-B at the Advanced Photon Source at Argonne National Laboratory. All measurements were performed at the Gd L_2 edge ($E = 7.938$ keV). An as-grown platelike single crystal was attached to a flat copper sample holder on the cold finger of a closed-cycle Joule-Thomson cryostat (the base temperature $T \approx 2$ K) and initially mounted to be $[1, 1, 0]$ within the scattering plane. By utilizing the six-circle diffractometer, we could rotate the sample azimuth angle to constrain $[0, 1, 0]$ in the scattering plane. The incident radiation was linearly polarized perpendicular to the vertical scattering plane (σ polarized). In this configuration, dipole resonant magnetic scattering rotates the scattered beam polarization into the scattering plane (π polarization), and the magnetic moment direction can be precisely determined. The magnetic moment components in the scattering plane (moment components projected onto the scattering plane) contribute to scattering intensity, while the magnetic moment components perpendicular to the scattering plane produce zero intensity. Scattered intensities were recorded using a two-dimensional detector. Throughout this paper, error bars represent one standard deviation.

III. RESULTS

Figure 1(b) presents the electrical resistivity of GdCuAs_2 . When the temperature is lowered, it first shows a typical metallic behavior, a decrease in resistivity. Then, we observe an increase in resistivity and a (local) resistivity minimum appearing at $T \approx 30$ K ($\equiv T_{\min}$). With further cooling, a sharp peak appears at $T = 10.6$ K ($\equiv T_{N_1}$). A close inspection at low temperatures reveals a slight change in slope below $T = 6$ K ($\equiv T_{N_2}$), implying an additional transition [Fig. 1(b)]. The absolute value of the resistivity of our single crystal is $6 \mu\Omega \text{ cm}$ at $T = 1.8$ K and the residual resistivity ratio (RRR) is 6.2, compared to $4500 \mu\Omega \text{ cm}$ and $\text{RRR} = 1.2$ measured in previous polycrystalline samples [26,27], indicating that the single crystal sample is of higher quality. Figure 1(c) presents the temperature-dependent resistivity measured under magnetic fields for $\mathbf{H} \parallel \mathbf{ab}$. The RM is suppressed as magnetic fields increase and disappears at $H = 9$ T. On the other hand, we observe a gradual decrease in the AFM transition temperature up to $H = 9$ T. This suggests that the electron scattering mechanism is coupled to the magnetism in the \mathbf{ab} plane.

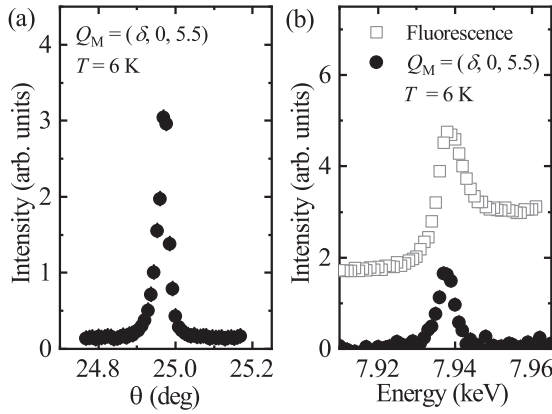


FIG. 2. Resonant magnetic scattering from the GdCuAs₂ single crystal. (a) Rocking (angle) scans θ through the $\mathbf{Q}_M = (\delta, 0, 5.5)$ magnetic peak position at $T = 6$ K. (b) Energy scan through the Gd L_2 absorption edge at the $\mathbf{Q}_M = (\delta, 0, 5.5)$ magnetic peak position at 6 K along with the measured x-ray fluorescence from the sample (open squares).

The magnetic susceptibility of GdCuAs₂ is plotted in Fig. 1(d) for both $\mathbf{H} \parallel \mathbf{ab}$ and $\mathbf{H} \parallel \mathbf{c}$ ($H = 1$ kOe). The high-temperature magnetic susceptibility (not shown) follows the Curie-Weiss (CW) law, resulting in CW temperature $\theta_{(\mathbf{H} \parallel \mathbf{ab})} \sim -12$ K and $\theta_{(\mathbf{H} \parallel \mathbf{c})} \sim -20$ K. The estimated effective moments of $\mu_{\text{eff}(\mathbf{H} \parallel \mathbf{ab})} = 8.13 \mu_B/\text{Gd}$ and $\mu_{\text{eff}(\mathbf{H} \parallel \mathbf{c})} = 8.00 \mu_B/\text{Gd}$ agree with the theoretical value. The sharp anomaly at $T = 10.6$ K ($\equiv T_{N_1}$) indicates the onset of a long-range AFM order. An

additional sharp change and bifurcation of zero-field-cooled and field-cooled magnetic susceptibility data appear below $T = 6.6$ K ($\approx T_{N_2}$), suggesting another magnetic transition at this temperature, consistent with the resistivity result.

Below T_{N_1} , the XRMS technique is used to determine the magnetic structure. As clearly shown in Fig. 2(a), Bragg scattering at $\mathbf{Q}_M = (\delta, 0, 5.5)$ confirms the AFM ordering, which is forbidden for the structural Bragg peak in the tetragonal crystal structure. The magnetic origin of this peak was also confirmed by energy scans through the Gd L_2 absorption edge. The energy scan [Fig. 2(b)] at the magnetic peak position shows typical magnetic scattering resonant enhancement [34]. The resonance primarily involves electric dipole ($E1$) transitions from the $2p_{3/2}$ core level to the empty $5d$ states, seen as the strong line just at or slightly below the maximum in the measured fluorescence intensity.

In Fig. 3(a), the rocking (angular) scans are plotted at two different Bragg peak positions: $\mathbf{Q}_M = (\delta, 0, 5.5)$ and $(0, \delta, 5.5)$. The scattering vector \mathbf{Q}_M is ensured to lie in the scattering plane for each measurement so that the magnetic moment component parallel to the scattering plane contributes to the signal. The XRMS intensity I_{XRMS} is proportional to the magnetic structure factor $F_m = \sum f_{\text{XRMS}} e^{2\pi i(hx_j + ky_j + lz_j)}$; $I_{\text{XRMS}} \propto |F_m|^2$. $f_{\text{XRMS}} \approx \mathbf{m} \cdot \mathbf{k}'$ is the resonant magnetic scattering amplitude, where \mathbf{k}' is the scattered beam vector and \mathbf{m} is the magnetic moment direction. The magnetic reflection at $(0, \delta, 5.5)$ was initially observed when the azimuth angle was set to include the $[1, 1, 0]$ direction in the scattering plane. Upon rotating the azimuth angle to align the $[0, 1, 0]$ direction within the scattering plane, $\mathbf{Q}_M = (0, \delta, 5.5)$ lies in

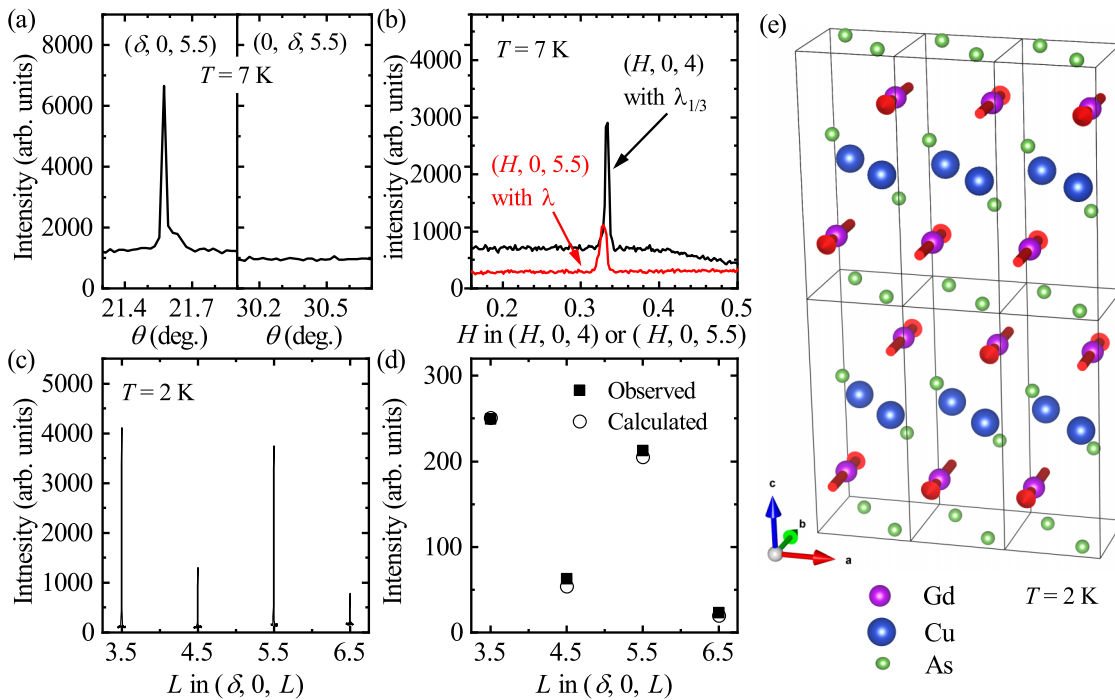


FIG. 3. (a) Rocking (angle) scans measured at $\mathbf{Q}_M = (\delta, 0, 5.5)$ (left) and $(0, \delta, 5.5)$ (right). (b) Comparison of \mathbf{Q} positions between the structure Bragg peak, $\mathbf{Q} = (1, 0, 12)$, measured with the third harmonics ($\lambda_{1/3}$) of the x ray and the magnetic Bragg peak, $\mathbf{Q}_M = (\delta, 0, 5.5)$, measured with the primary x ray (λ). (c) L dependence of magnetic Bragg peak $\mathbf{Q}_M = (\delta, 0, L)$. (d) Calculated vs measured magnetic Bragg peak intensities for $L = 3.5-6.5$. All measurements in (c) and (d) were performed at $T = 2$ K. (e) Magnetic structure of GdCuAs₂ at $T = 2$ K for $\mathbf{q} = (\delta, 0, 0.5)$ with $\delta = 1/3$. This figure was created using the VESTA program [35].

TABLE I. Magnetic representations (MRs) for GdCuAs₂ for space group $P4/nmm$ with propagation vector $(1/3, 0, 0.5)$. The decomposition of the MR for Gd site $(0.25, 0.25, 0.23844)$ is $\Gamma_{\text{mag}} = \Gamma_1 + 2\Gamma_2 + \Gamma_3 + 2\Gamma_4$. The atoms of the primitive basis are defined according to (1) $(0.25, 0.25, 0.23844)$ and (2) $(0.75, 0.75, 0.76156)$. Real (C_R) and imaginary (C_I) numbers in the basis vector (BV) component determine the magnetic moment direction at the atom with $\mathbf{m} \approx C_R \cos 2\pi \mathbf{k} \cdot \mathbf{R} + C_I \sin 2\pi \mathbf{k} \cdot \mathbf{R}$, where \mathbf{k} and \mathbf{R} are the reciprocal space and real space lattice vectors, respectively. IR stands for irreducible representation.

IR	Atom	BV components		
		$m \parallel a$	$m \parallel b$	$m \parallel c$
Γ_1	1	2	0	0
	2	$1 - 1.732i$	0	0
Γ_2	1	0	2	0
	2	0	$-1 + 1.732i$	0
Γ_2	1	0	0	2
	2	0	0	$1 - 1.732i$
Γ_3	1	2	0	0
	2	$-1 + 1.732i$	0	0
Γ_4	1	0	2	0
	2	0	$1 - 1.732i$	0
Γ_4	1	0	0	2
	2	0	0	$-1 + 1.732i$

the $(0, K, L)$ scattering plane. In this configuration, the Gd moments within the scattering plane (the components along the \mathbf{b} and \mathbf{c} directions) contribute to the XRMS intensity. The absence of intensity at $\mathbf{Q}_M = (0, \delta, 5.5)$ in Fig. 3(a) indicates that the Gd moments are oriented in neither the \mathbf{b} nor the \mathbf{c} direction. They are perpendicular to the magnetic propagation vector, which is in the \mathbf{a} axis. In contrast, in the rocking scan at $\mathbf{Q}_M = (\delta, 0, 5.5)$ at this azimuth, the direction of the Gd moments is perpendicular to the propagation vector $\mathbf{Q}_M = (\delta, 0, 5.5)$, which is along the \mathbf{b} axis. Since the moments lie in the scattering plane, the XRMS intensity is observed at $\mathbf{Q}_M = (\delta, 0, 5.5)$.

The magnetic peak appears at δ close to $1/3$ at $T \approx 7$ K. To check the incommensurability of the magnetic ordering, the structural Bragg peak $\mathbf{Q} = (1, 0, 12)$ is measured using the third harmonic component of the x ray ($\lambda_{1/3}$). We see the $(1, 0, 12)$ peak appearing at the $(1/3, 0, 4)$ position, as shown in Fig. 3(b). On the other hand, the magnetic peak appears at a slightly lower value of $H = 0.330$, indicating that the true magnetic wave vector is $\mathbf{Q}_M = (0.330, 0, 5.5)$ at this temperature. This concludes the AFM incommensurate magnetic modulation in the \mathbf{a} axis with the Gd moment pointing along the \mathbf{b} axis, with the FM arrangement along the \mathbf{b} axis.

To determine the magnetic ordering along the \mathbf{c} axis, we measure the L dependence of the magnetic Bragg peaks shown in Figs. 3(c) and 3(d) and compare it to our representation analysis [36]. Table I shows six magnetic representations (MRs) calculated for the $P4/nmm$ space group and the $(1/3, 0, 0.5)$ propagation vector for the Gd order. Our experimental observation of the Gd moments along the \mathbf{b} axis, perpendicular to the propagation along $[\delta, 0, 0.5]$, excludes basis vectors with the \mathbf{a} and \mathbf{c} axis components of the Gd moment,

eliminating MRs Γ_1, Γ_2 with $\mathbf{m} \parallel \mathbf{c}$, Γ_3 , and Γ_4 with $\mathbf{m} \parallel \mathbf{c}$. Furthermore, MRs Γ_2 and Γ_4 with $\mathbf{m} \parallel \mathbf{b}$ are distinguished by their arrangement of moments along the \mathbf{c} axis. The Gd moments are antiferromagnetically arranged as $(+ - + -)$ along the \mathbf{c} axis in MR Γ_2 and as $(+ + - -)$ in Γ_4 . These two different \mathbf{c} -axis arrangements yield different peak intensities. The observed L dependence of the magnetic peak intensities in Fig. 3(c) matches the XRMS intensity calculation for the $(+ + - -)$ arrangement of the moments along the \mathbf{c} axis [Fig. 3(d)]. We plot the determined magnetic structure of GdCuAs₂ at $T = 2$ K in Fig. 3(e). The Gd moments pointing in the \mathbf{b} axis align antiferromagnetically (ferromagnetically) in the \mathbf{a} (\mathbf{b}) axis, with the \mathbf{c} -axis arrangement being $(+ + - -)$. This results in $\mathbf{q} = (1/3, 0, 0.5)$. We note that the determined magnetic structure is different from that of previously reported $RCuAs_2$ sister compounds [33].

The intensity and peak position of the magnetic Bragg peak are investigated as a function of temperature. Figure 4(a) shows the \mathbf{Q} scans along the H direction at $(\delta, 0, 5.5)$ at selected temperatures, where both Bragg peak positions and intensities are clearly dependent on temperature. Figure 4(b) displays the integrated intensity of the magnetic Bragg peak as a function of temperature, where the intensity grows as the temperature is lowered. The magnetic signal appears below 10 K, and an additional increase in intensity is observed at around 6 K, which is well aligned with the resistivity and magnetization measurements. The position of the magnetic peak is plotted in Fig. 4(c) as a function of the temperature. The magnetic peak first appears at $\delta \approx 0.3305$ at $T = 9.5$ K. With further cooling, δ decreases and reaches its minimum at $T \approx 8$ K, then increases approaching $1/3$. At $T_{N_2} \approx 6$ K, the magnetic peak locks into the commensurate position $\delta = 1/3$, and the magnetic structure remains commensurate down to the base temperature of our measurement.

Utilizing the high-resolution SXD, we study the lattice parameters as a function of the temperature below $T \leq 60$ K, which are presented in Figs. 5 and 6. Raw θ - 2θ scans at $\mathbf{Q} = (0, 0, 8)$ are shown for selected temperatures in Figs. 5(a) and 5(c). We note that a slight asymmetry in the peak shape is observed, which may be caused by a slight misalignment between crystallites or off-stoichiometry variations in the sample volume. The very small angle distribution and the sharp transition in resistivity and magnetization data suggest that off-stoichiometry variations are unlikely to cause the observed asymmetry. In addition, the powder x-ray and energy dispersive x-ray measurements indicate no evidence of off-stoichiometry variations within the instrumental error. We fit the data using a Voigt peak function to account for the asymmetric peak shape, as shown in Fig. 5(c), and determine lattice parameter c in Fig. 6(a). Lattice parameter c decreases quasilinearly with temperature and reaches a plateau around $T = 30$ K, coincident with T_{min} . The plateau remains down to ≈ 10 K (T_{N_1}), which can also be seen as a slight increase. Then, a small drop in lattice parameter c is observed just below T_{N_1} , followed by a slight expansion of the unit cell below T_{N_2} . Changes in lattice parameter c below 10 K are emphasized in the inset of Fig. 6(a). The changes in lattice parameter c below 30 K are very small, but the changes occur at characteristic temperatures T_{min} , T_{N_1} , and T_{N_2} , indicating that these are intrinsically coupled to the lattice.

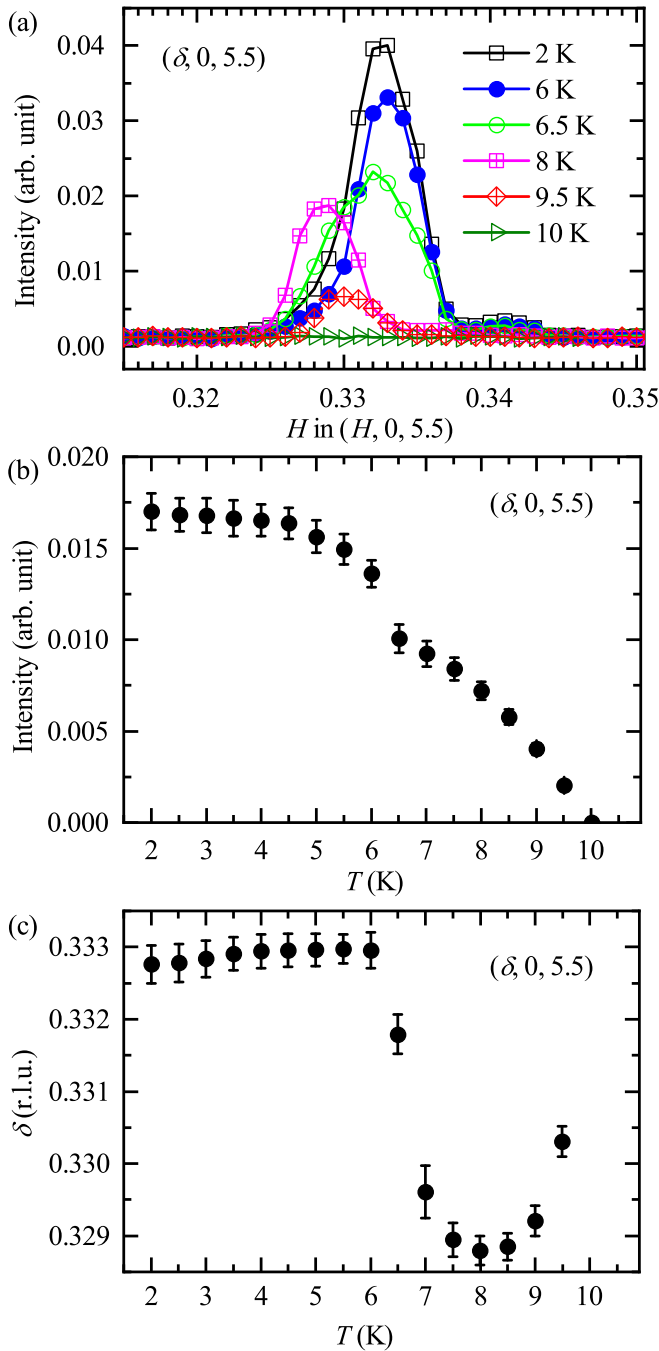


FIG. 4. (a) Magnetic Bragg peaks at $\mathbf{Q}_M = (\delta, 0, 5.5)$ at selected temperatures. (b) Antiferromagnetic order parameter obtained from the integrated intensity of $\mathbf{Q}_M = (\delta, 0, 5.5)$ Bragg peaks. (c) Peak positions of $\mathbf{Q}_M = (\delta, 0, 5.5)$ obtained from fitting the data with the Voigt line shapes.

Figure 5(b) presents raw θ - 2θ scans at $\mathbf{Q} = (2, 0, 6)$. Interestingly, a distinct shoulder next to the expected $(2, 0, 6)$ peak position is detected at $T = 60$ K. As the temperature is lowered, the shoulder disappears at around $T = 25$ K, becoming one broad peak. By further cooling, the peak remains sharper down to the base temperature of $T = 2$ K. Changes in the shape of the peak can indicate a possible structural change associated with more than one peak at the measured \mathbf{Q} . We attempt to fit the curve with two Lorentzian-squared peak

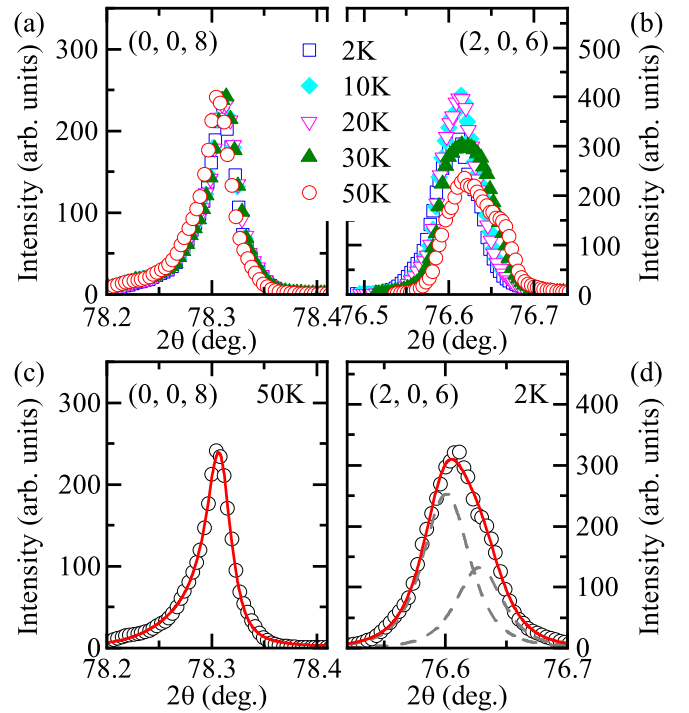


FIG. 5. θ - 2θ scans at (a) $\mathbf{Q} = (0, 0, 8)$ and (b) $\mathbf{Q} = (2, 0, 6)$ at selected temperatures. (c) Our fit using the asymmetric Voigt peak function (red line) is shown with the scan at $\mathbf{Q} = (0, 0, 8)$ at $T = 50$ K (symbols). (d) Fitting with two Lorentzian-squared peaks is plotted on top of the scan at $\mathbf{Q} = (2, 0, 6)$ at $T = 2$ K. The red line indicates the overall fit, and the gray dashed lines show the two peaks used in the fitting.

shape functions for higher temperatures and one Lorentzian-squared peak shape function for low temperature. One-peak fitting yields broader peaks at low temperatures compared to the peak width at higher temperatures by two-peak fitting. On the other hand, when all the data are fit with two peak shape functions, their peak widths are consistent in all temperature range. Thus, we fit the data with two Lorentzian-squared peak shape functions, as shown in Fig. 5(d). The corresponding lattice parameters are shown in Fig. 6(b), where lattice parameters a (circles) and b (triangles) are determined by the convention $a < b$. Both lattice parameters a and b decrease monotonously below $T = 60$ K and then increase rapidly below $T = 30$ K ($\approx T_{\min}$), followed by a slow increase below $T = 20$ K. These changes in the lattice parameters coincide with the change in the peak shape. Note that because our lattice parameter measurements at $\mathbf{Q} = (2, 0, 6)$ were performed with large temperature steps, we were not able to determine possible changes in lattice parameter a at T_{N_1} and T_{N_2} . The observation of two peaks at $\mathbf{Q} = (2, 0, 6)$ suggests a lower-symmetry crystal structure than the reported tetragonal structure.

IV. DISCUSSION AND SUMMARY

High-resolution SXD measurements, resulting in different lattice parameters a and b , suggest that the crystal structure of GdCuAs_2 has a lower symmetry than the reported tetragonal structure. The orthorhombic distortion, defined as

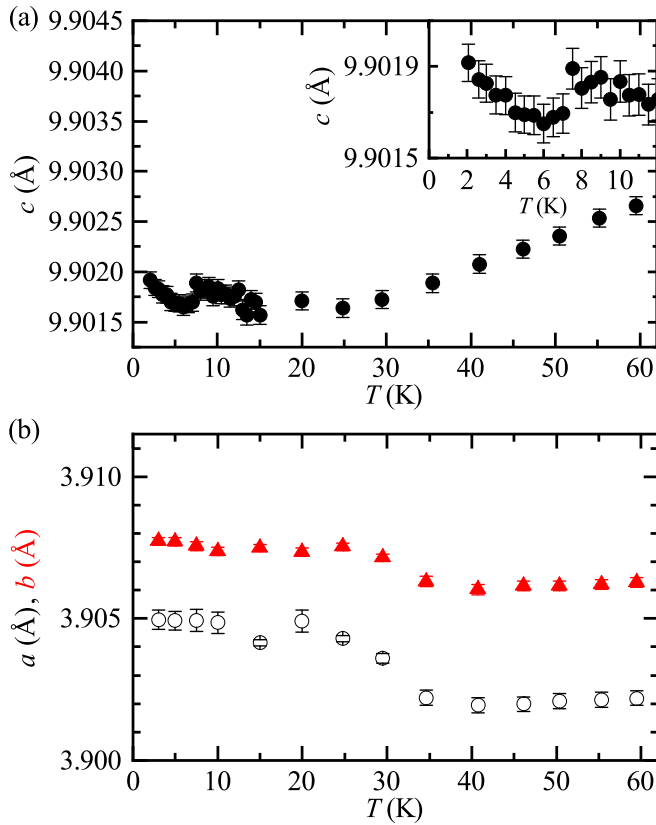


FIG. 6. (a) Lattice parameter c , obtained from the fit of the data described in the text. The inset shows the temperature range below $T = 12$ K. (b) Lattice parameters a and b (circles and triangles, respectively) from a two-peak fitting with Lorentzian-squared line shapes. See the details in the text.

$(a - b)/(a + b)$, is very small, approximately 0.0005 at $T = 60$ K in our sample. Although one study on polycrystalline samples claimed a monoclinic $P12_1/m1$ for GdCuAs_2 [32], the proposed Peierls distortion might be too small to detect with powder x-ray diffraction measurements. Our use of synchrotron x-ray radiation together with a high-quality single crystal provides an angular resolution of better than 0.05° and allows us to observe small distortions embedded in this compound. However, such a small distortion can be enhanced by doping, as shown from the orthorhombic ($Pm\bar{m}n$) structure for $\text{GdCu}(\text{As}_{1-x}\text{P}_x)_2$ [29,30], where $(a - b)/(a + b) \approx 0.0009$ for $\text{GdCu}(\text{As}_{0.835}\text{P}_{0.165})_2$, becoming measurable with powder x-ray diffraction. Thus, we conjecture that the crystal structure of GdCuAs_2 is likely the orthorhombic $Pm\bar{m}n$ structure shown in its sister compounds. Since thermodynamic and transport property measurements above T_{N_1} indicate no anomalies related to the structural phase transition, the crystal structure of GdCuAs_2 is expected to be in the orthorhombic structure at all temperatures studied. The orthorhombic distortion naturally provides anisotropy in the ab plane that is favorable for the Gd spin to choose its direction. This is consistent with our observation of the magnetic structure, as shown in Fig. 3(e).

We determined the magnetic structure unambiguously with our XRMS measurements, which implies that the magnetic interactions are FM in the b direction and AFM in the a and c directions with the $(\delta, 0, 0.5)$ propagation vector. Strong

magnetoelastic coupling can promote lattice expansion or contraction, depending on the type of magnetic interactions. Earlier mean-field studies on magnetoelastic coupling, leading to nematic order, showed that a lattice contraction occurs along the direction where the interaction is FM and a lattice expansion occurs when the interaction is AFM [37,38]. For GdCuAs_2 , the observed lattice distortion is smaller at $T = 2$ K than at $T = 40$ K. The reduced distortion at $T = 2$ K can naturally be explained by the lattice expansion on the a axis where the AFM interaction persists and the simultaneous lattice contraction on the b axis with the FM interaction, consequently reducing their difference. It is interesting to think that the nematic order, which has received much attention in Fe-based superconductors, could be responsible for the additional reduction in the distortion below 30 K in GdCuAs_2 . Further studies, e.g., strain experiments, will shed light on this hypothesis. It is worth mentioning that the magnetic structure of GdCuAs_2 is different from the magnetic structures of RCuAs_2 determined by powder neutron diffraction. It is noticeably different from the complex magnetic structure of TbCuAs_2 , although one can expect GdCuAs_2 and TbCuAs_2 to have some similarities because Gd and Tb are right next to each other in the periodic table. The difference in the magnetic structures may be intrinsic or led by unknown factors involved in sample preparation.

A thermodynamic model study can also explain changes in the lattice parameters, especially volume expansion, at low temperatures. The model suggests a negative thermal expansion at the onset of the Néel transition due to the reduction in the magnetic pressure by the long-range RKKY interaction in the ordered state [39]. However, GdCuAs_2 shows changes in the lattice parameters, resembling negative thermal expansion, well above T_{N_1} and around T_{min} . In this temperature range, the RKKY interaction can be sufficiently long but small enough not to induce a long-range AFM order and lead to negative thermal-expansion-like lattice behaviors.

Interestingly, the magnetic polaron formation has been considered as a mechanism for the resistivity minimum in a few materials, such as EuB_6 , Gd_2PdSi_3 , and EuIn_2As_2 [21–24]. Localization of electrons via exchange interaction and magnetic polaron formation can yield additional electron scatterings at low temperatures. While such a mechanism may not be applicable to the good metal GdCuAs_2 , together with the above-mentioned thermodynamic RKKY model, it implies that the magnetic interaction plays a crucial role not only in the electrical resistivity but also in the crystal lattice.

The magnetic-field dependence of the resistivity minimum [Fig. 1(c)] suggests an intimate coupling between resistivity and magnetism well above the AFM ordering temperature. The electron scattering mechanism may be strongly influenced by the magnetism in the ab plane. The leading spin Hamiltonian is the magnetic interaction with conduction electrons, which can be greatly modified by external magnetic fields. Therefore, all ties together and provides evidence that the magnetic interaction well above T_{N_1} plays a crucial role in the appearance of the resistivity minimum and the lattice distortion in GdCuAs_2 . An investigation of Gd spin interactions in the form of spin fluctuations is necessary to understand this matter deeply.

ACKNOWLEDGMENTS

This work was supported by the University of Wisconsin–Milwaukee. M.G.K. acknowledges valuable discussions with T. Shishidou, M. Weinert, and D. Agterberg. This research used resources from the Advanced Photon Source, a U.S. Department of Energy (DOE) Office of Science

User Facility operated for the DOE Office of Science by Argonne National Laboratory under Contract No. DE-AC02-06CH11357. E.D.M. was supported by the Canada Research Chairs, Natural Sciences and Engineering Research Council of Canada, and Canada Foundation for Innovation program.

-
- [1] N. W. Ashcroft and N. D. Mermin, *Solid State Physics* (Saunders College, Philadelphia, 1976).
- [2] C. Kittel, *Introduction to Solid State Physics*, 8th ed. (Wiley, New York, 2004).
- [3] M. Tinkham, *Introduction to Superconductivity*, 2nd ed. (Dover, 2004).
- [4] M. R. Norman, *Science* **332**, 196 (2011).
- [5] J. Kondo, *Prog. Theor. Phys.* **32**, 37 (1964).
- [6] J. S. Dugdale, *The Electrical Properties of Metals and Alloys* (Edward Arnold, London, 1977), p. 292.
- [7] A. C. Hewson, *The Kondo Problem to Heavy Fermions*, Cambridge Studies in Magnetism (Cambridge University Press, Cambridge, 1993).
- [8] A. Edelstein, *Phys. Lett. A* **27**, 614 (1968).
- [9] S. Chakraborty and A. K. Majumdar, *Phys. Rev. B* **53**, 6235 (1996).
- [10] R. W. Cochrane and J. O. Strom-Olsen, *Phys. Rev. B* **29**, 1088 (1984).
- [11] A. Das and A. K. Majumdar, *Phys. Rev. B* **43**, 6042 (1991).
- [12] S. N. Kaul, W. Kettler, and M. Rosenberg, *Phys. Rev. B* **33**, 4987 (1986).
- [13] T. K. Nath and A. K. Majumdar, *Phys. Rev. B* **55**, 5554 (1997).
- [14] E. Rozenberg, M. Auslender, I. Felner, and G. Gorodetsky, *J. Appl. Phys.* **88**, 2578 (2000).
- [15] M. Ziese, *Phys. Rev. B* **68**, 132411 (2003).
- [16] Y. Jin, X.-P. Cui, W.-H. Han, S.-X. Cao, Y.-Z. Gao, and J.-C. Zhang, *Phys. Chem. Chem. Phys.* **17**, 12826 (2015).
- [17] B. Li, H. Zhu, Q. Liu, Z. Liu, and Y. Zhang, *J. Magn. Magn. Mater.* **366**, 50 (2014).
- [18] D. Kumar, J. Sankar, J. Narayan, R. K. Singh, and A. K. Majumdar, *Phys. Rev. B* **65**, 094407 (2002).
- [19] K. Das, B. Satpati, and I. Das, *RSC Adv.* **5**, 27338 (2015).
- [20] Y. Matsushita, H. Bluhm, T. H. Geballe, and I. R. Fisher, *Phys. Rev. Lett.* **94**, 157002 (2005).
- [21] P. Nyhus, S. Yoon, M. Kauffman, S. L. Cooper, Z. Fisk, and J. Sarrao, *Phys. Rev. B* **56**, 2717 (1997).
- [22] R. Mallik, E. V. Sampathkumaran, M. Strecker, and G. Wortmann, *Europhys. Lett.* **41**, 315 (1998).
- [23] J. Chatterjee, U. Yu, and B. I. Min, *Phys. Rev. B* **69**, 134423 (2004).
- [24] Y. Zhang, K. Deng, X. Zhang, M. Wang, Y. Wang, C. Liu, J.-W. Mei, S. Kumar, E. F. Schwier, K. Shimada, C. Chen, and B. Shen, *Phys. Rev. B* **101**, 205126 (2020).
- [25] Z. Wang, K. Barros, G.-W. Chern, D. L. Maslov, and C. D. Batista, *Phys. Rev. Lett.* **117**, 206601 (2016).
- [26] E. V. Sampathkumaran, K. Sengupta, S. Rayaprol, K. K. Iyer, T. Doert, and J. P. F. Jemetio, *Phys. Rev. Lett.* **91**, 036603 (2003).
- [27] K. Sengupta, S. Rayaprol, E. Sampathkumaran, T. Doert, and J. Jemetio, *Physica B (Amsterdam, Neth.)* **348**, 465 (2004).
- [28] D. Evans, Master's thesis, Simon Fraser University, 2021.
- [29] Y. Mozharivskiy, D. Kaczorowski, and H. F. Franzen, *J. Solid State Chem.* **155**, 259 (2000).
- [30] Y. Mozharivskiy and H. F. Franzen, *J. Phys. Chem. B* **106**, 9528 (2002).
- [31] J.-P. Jemetio, T. Doert, O. Rademacher, and P. Böttcher, *J. Alloys Compd.* **338**, 93 (2002).
- [32] D. Rutzinger, C. Bartsch, T. Doert, and M. Ruck, *Acta Crystallogr. Sect. B* **65**, 527 (2009).
- [33] Y. Zhao, J. Lynn, G. Thakur, Z. Haque, L. Gupta, and A. Ganguli, *J. Phys. Chem. Solids* **111**, 1 (2017).
- [34] J. W. Kim, Y. Lee, D. Wermeille, B. Sieve, L. Tan, S. L. Bud'ko, S. Law, P. C. Canfield, B. N. Harmon, and A. I. Goldman, *Phys. Rev. B* **72**, 064403 (2005).
- [35] K. Momma and F. Izumi, *J. Appl. Crystallogr.* **44**, 1272 (2011).
- [36] A. Wills, *Physica B (Amsterdam, Neth.)* **276–278**, 680 (2000).
- [37] R. M. Fernandes, D. K. Pratt, W. Tian, J. Zarestky, A. Kreyssig, S. Nandi, M. G. Kim, A. Thaler, N. Ni, P. C. Canfield, R. J. McQueeney, J. Schmalian, and A. I. Goldman, *Phys. Rev. B* **81**, 140501(R) (2010).
- [38] R. M. Fernandes, L. H. VanBebber, S. Bhattacharya, P. Chandra, V. Keppens, D. Mandrus, M. A. McGuire, B. C. Sales, A. S. Sefat, and J. Schmalian, *Phys. Rev. Lett.* **105**, 157003 (2010).
- [39] T. Balcerzak, K. Szałowski, and M. Jaščr, *J. Magn. Magn. Mater.* **452**, 360 (2018).